Validation of the Full-Wave Projector-Based Hamiltonian Analysis of Port-Driven Microwave Resonators

S. Moon and **T. E. Roth**

Elmore Family School of Electrical and Computer Engineering, Purdue University, West Lafayette, Indiana, USA

Abstract— Quantum information processing technologies are gaining interest due to their potential for performance exceeding what is possible with the best classical computers. One of the most promising platforms is the circuit quantum electrodynamics (cQED) architecture that controls superconducting circuit qubits by coupling them to electromagnetic fields in microwave resonators or waveguides. As these devices become increasingly complex, existing analysis and design approaches that often rely on lumped element circuit approximations can become inadequate due to their lack of accuracy and flexibility. This is leading to a growing interest in developing quantum full-wave numerical modeling methods for the high-fidelity analysis of cQED devices. In this work, we focus on a quantum full-wave modeling approach that uses a projector-based quantization approach that allows a problem to be decomposed into distinct subdomains whose fields can be quantized more easily. This leads to a framework that can naturally incorporate microwave ports, which is not straightforward with other formulations. Here, we consider an explicit problem of a coaxial-fed rectangular waveguide cavity to validate parts of our projector-based formalism. Toward this end, we apply this approach to a classical Hamiltonian analysis of this system that can be used to more easily validate the relevant full-wave aspects of the corresponding quantum formulation. In addition to presenting the formulation of the full-wave classical Hamiltonian of the system, we derive equations of motion and discuss an analytical solution procedure with an input-output theory approach. We validate our formulation by comparing the input-output theory results to standard finite element method (FEM) scattering parameter simulations.

1. INTRODUCTION

Quantum information processing devices are revolutionary technologies that have the potential to leverage quantum effects to achieve unparalleled performance compared to conventional technology. One particularly promising platform is the circuit quantum electrodynamics (cQED) architecture, as demonstrated through recent landmark achievements of a computational advantage over the most powerful classical machines [1, 2]. However, there is still a gap to achieving practical quantum computation, which requires significant improvement in the performance of each component of these systems while also massively scaling the number of qubits involved [3, 4].

Tackling these engineering challenges will result in increased hardware complexity, which stresses the deficiencies in existing analysis methods and emphasizes the need for new high-fidelity modeling approaches to be developed. Most often, systems are initially conceptualized and analyzed using simplified lumped-element circuit descriptions [5]. The fidelity of these simplified models are limited due to their omission of various frequency- and spatial-dependent effects, which can lead to significantly incorrect modeling predictions [6]. To address some of these issues, black-box circuit quantization techniques were introduced to incorporate the effects of more modes of an electromagnetic system into a lumped-element circuit model [7]. Although these methods do utilize full-wave results in building their circuit models, the process involves inconvenient curve-fitting procedures that become impractical when including many modes of the electromagnetic system. More recently, quantum full-wave modeling approaches that more directly work with electromagnetic eigenmodes are gaining interest for achieving accurate solutions in the design of cQED devices [8, 9].

In this work, we focus on the projector-based quantization technique from [9] due to its superior handling of ports in the description of an electromagnetic system, as well as its potential for developing domain decomposition methods that produce more intuitively-useful numerical results. Here, we validate field-dependent parameters of this model by investigating a classical version of the formulation which can be more easily verified by comparing to widely-available classical full-wave simulation tools. To achieve this, we begin in Section 2 by introducing the classical projector-based Hamiltonian analysis approach, with additional details on normalizing the relevant eigenmodes

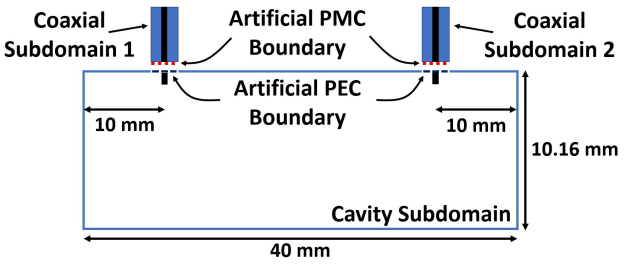

Figure 1: Schematic illustration of the subdomains for the projector-based full-wave Hamiltonian analysis of a coaxial-fed rectangular waveguide cavity.

included in an appendix. In Section 3, we derive the equations of motion for this system and then solve them using the analytical input-output theory approach commonly used in quantum optics. Following this, we demonstrate the validation of our approach through numerical results in Section 4. Finally, we discuss conclusions and future work in Section 5.

2. FORMULATION

One quantization approach particularly suited to a geometry like that in Fig. 1 is the projector-based quantization method used in [9]. In this approach, the entire system is decomposed into different subdomains by introducing artificial boundary conditions at the interface of each region. Each subdomain is terminated by complementary boundary conditions of either perfect electric conductor (PEC) or perfect magnetic conductor (PMC) at the interface. This maintains the hermiticity of the eigenvalue problem of each region, which guarantees that a complete set of orthonormal eigenmodes can be found and then used to represent the fields in each subdomain. With the field descriptions isolated in the spatial bound of each subdomain, the physical dynamics between subdomains must be tied together to recover the solution to the original problem. More details on the specifics of this can be found in [9], but the end result is that the strength of coupling between modes in different regions is proportional to the spatial overlap integral of the field mode profiles over the interface surface between subdomains. The final result is the system and bath Hamiltonian commonly used in quantum optics [10], but with the important distinction that all Hamiltonian parameters can be computed *a priori* rather than relying on curve fitting to measured data or other similar procedures.

We now consider the explicit case of applying the projector-based approach to formulating a classical Hamiltonian analysis of the geometry shown in Fig. 1. In our expressions, we allow for a spatially-varying permittivity, but assume there are no magnetic materials present. In this case, the fields of each subdomain are solutions to the wave equation

$$\nabla \times \nabla \times \mathbf{E}(\mathbf{r},t) + \mu\epsilon\partial_t^2 \mathbf{E}(\mathbf{r},t) = 0. \tag{1}$$

We use the separation of variables approach beginning in the cavity subdomain according to

$$\mathbf{E}_q(\mathbf{r},t) = \sum_k \sqrt{\frac{\omega_k}{\epsilon_0}} q_k(t)\mathbf{E}_k(\mathbf{r}), \tag{2}$$

which separates the spatial eigenmodes $\mathbf{E}_k(\mathbf{r})$ and the temporal amplitude $q_k(t)$ for a particular eigenvalue ω_k. For this kind of solution, we find the separated equations

$$\partial_t^2 q_k(t) = -\omega_k^2 q_k(t), \tag{3}$$

$$\nabla \times \nabla \times \mathbf{E}_k(\mathbf{r}) - \mu\epsilon\omega_k^2 \mathbf{E}_k(\mathbf{r}) = 0. \tag{4}$$

The magnetic field can be expanded similarly and is given as

$$\mathbf{H}_q(\mathbf{r},t) = \sum_k \sqrt{\frac{\omega_k}{\mu_0}} p_k(t)\mathbf{H}_k(\mathbf{r}), \tag{5}$$

where p_k is the canonical conjugate to q_k in a Hamiltonian framework. It is common to combine these conjugate amplitudes into a single complex-valued amplitude as

$$a_k(t) = \frac{1}{\sqrt{2}}(q_k(t) + ip_k(t)). \tag{6}$$

After substituting this into (2) and (5), we get

$$\mathbf{E}_q(\mathbf{r}, t) = \sum_k \sqrt{\frac{\omega_k}{2\epsilon_0}}\big(a_k(t) + a_k^*(t)\big)\mathbf{E}_k(\mathbf{r}), \tag{7}$$

$$\mathbf{H}_q(\mathbf{r}, t) = -i\sum_k \sqrt{\frac{\omega_k}{2\mu_0}}\big(a_k(t) - a_k^*(t)\big)\mathbf{H}_k(\mathbf{r}). \tag{8}$$

Typically, it is convenient to work with field modes that are orthonormal. In this case, the sense of orthonormality is given by

$$\iiint \epsilon_r(\mathbf{r})\mathbf{E}_{k_1}^*(\mathbf{r}) \cdot \mathbf{E}_{k_2}(\mathbf{r})d\mathbf{r} = \delta_{k_1,k_2}, \tag{9}$$

where δ_{k_1,k_2} is the Kronecker delta function. The practical aspects of this is detailed in the appendix.

For fields in the pth coaxial subdomain, there is a continuum of modes due to its semi-infinite length so the expansion becomes

$$\mathbf{E}_p(\mathbf{r}, t) = \sum_\lambda \int_0^\infty \sqrt{\frac{\omega_{\lambda p}}{2\epsilon_0}}\big(a_{\lambda p}(t, \omega_{\lambda p}) + a_{\lambda p}^*(t, \omega_{\lambda p})\big)\mathbf{E}_{\lambda p}(\mathbf{r}, \omega_{\lambda p})\, d\omega_{\lambda p}, \tag{10}$$

where p indexes the coaxial subdomains and λ differentiates between transverse mode profiles with corresponding eigenvalues $\omega_{\lambda p}$. The definition of $a_{\lambda p}(t, \omega_{\lambda p})$ and $\mathbf{H}_p$ follow the format of the cavity fields, adjusted for the continuum of modes. The orthonormality condition must also be adjusted, and is now

$$\iiint \epsilon_r(\mathbf{r})\mathbf{E}_{\lambda_1 p}^*(\mathbf{r}, \omega_{\lambda_1 p}) \cdot \mathbf{E}_{\lambda_2 p}(\mathbf{r}, \omega'_{\lambda_2 p})d\mathbf{r} = \delta_{\lambda_1,\lambda_2}\delta(\omega_{\lambda_1 p} - \omega'_{\lambda_2 p}), \tag{11}$$

The details for the field mode normalization expressions for coaxial fields can be found in the appendix as well.

These mode expansions may now be substituted into the full projector-based Hamiltonian, which here is

$$H_T = H_Q + H_P + H_{QP}. \tag{12}$$

The terms in (12) are given as [9]

$$H_Q = \iiint \frac{1}{2}\big(\epsilon|\mathbf{E}_q(\mathbf{r}, t)|^2 + \mu|\mathbf{H}_q(\mathbf{r}, t)|^2\big)d\mathbf{r}, \tag{13}$$

$$H_P = \sum_p \iiint \frac{1}{2}\big(\epsilon|\mathbf{E}_p(\mathbf{r}, t)|^2 + \mu|\mathbf{H}_p(\mathbf{r}, t)|^2\big)d\mathbf{r}, \tag{14}$$

$$H_{QP} = -\sum_p \iiint \mathbf{F}_q(\mathbf{r}, t) \cdot \big(\mathbf{E}_p(\mathbf{r}, t) \times \hat{n}_p\big)d\mathbf{r}, \tag{15}$$

where the electric vector potential in the cavity subdomain is

$$\mathbf{F}_q(\mathbf{r}, t) = -\sum_k \sqrt{\frac{1}{\omega_k\mu_0}}q_k(t)\mathbf{H}_k(\mathbf{r}). \tag{16}$$

By substituting the field expansions into (13) to (15), each Hamiltonian term can be simplified using the eigenmode orthonormality. For the cavity and coaxial subdomains, the Hamiltonians become

$$H_Q = \sum_k \omega_k a_k^* a_k, \tag{17}$$

$$H_P = \sum_{p,\lambda} \int_0^\infty \omega_{\lambda p} a_{\lambda p}^*(t, \omega_{\lambda p}) a_{\lambda p}(t, \omega_{\lambda p}) d\omega_{\lambda p}. \tag{18}$$

The remaining Hamiltonian represents interactions between fields in different subdomains, which for this case becomes

$$H_{QP} = \sum_{k,p,\lambda} \int_0^\infty g_{k,\lambda p}(a_k + a_k^*)(a_{\lambda p} + a_{\lambda p}^*) d\omega_{\lambda p}, \tag{19}$$

$$g_{k,\lambda p} = \iint \frac{c_0}{2} \sqrt{\frac{\omega_{\lambda p}}{\omega_k}} \left[\mathbf{H}_k \cdot (\mathbf{E}_{\lambda p} \times \hat{n}_p)\right] dS, \tag{20}$$

where the surface integration occurs over the interface between subdomains and $\hat{n}_p$ is the unit normal pointing into the cavity.

3. INPUT-OUTPUT THEORY

In this section, we provide the formulation of the equations of motion and then solve them using a classical version of input-output theory [11]. An equation of motion for an arbitrary a can be derived by taking a Poisson bracket with the total Hamiltonian, i.e.,

$$\frac{\partial a}{\partial t} = \{a, H_T\}, \tag{21}$$

where the Poisson bracket is defined as

$$\{f, g\} = \sum_i \left(\frac{\partial f}{\partial q_i} \frac{\partial g}{\partial p_i} - \frac{\partial f}{\partial p_i} \frac{\partial g}{\partial q_i} \right) \tag{22}$$

for f and q that are functions of the canonical conjugates q_i and p_i defined for a particular ith discrete eigenmode (this definition can be generalized to the continuum case in a straightforward manner). Due to the definition, the Poisson brackets will only be non-zero for variables associated with the same eigenmode. Overall, one is able to find that

$$\{a_k(t), a_{k'}^*(t)\} = -i\delta_{k,k'}, \tag{23}$$

$$\{a_{\lambda p}(t, \omega_{\lambda p}), a_{\lambda' p'}(t, \omega'_{\lambda' p'})\} = -i\delta_{\lambda,\lambda'}\delta_{p,p'}\delta(\omega_{\lambda p} - \omega'_{\lambda' p'}), \tag{24}$$

while the Poisson bracket for the variables between different regions results in a zero value.

To apply input-output theory, we will first simplify the formulation so that it remains analytically tractable. In particular, we will apply the rotating wave approximation and restrict our analysis to only consider the dominant cavity mode (with complex-valued amplitude denoted as a_0) and the continuum of TEM modes in the coaxial subdomains (denoted as a_p). Further, we will assume the field solutions are narrowband such that it is possible to extend the frequency integration range to $-\infty$ (this allows certian useful results from Fourier theory to be used) [11]. With these restrictions, the equations of motion are

$$\frac{\partial a_0}{\partial t} = -i\omega_0 a_0 - i \sum_p \int_{-\infty}^\infty g_p a_p d\omega_p, \tag{25}$$

$$\frac{\partial a_p}{\partial t} = -i\omega_p a_p - ig_p a_0, \tag{26}$$

where g_p is the restriction of (20) to the modes specified above.

The next step in input-output theory is to integrate the equations of motion in the coaxial subdomains in terms of initial and final conditions, which are taken to be well before and well after the interaction with the cavity has occurred so that they can be considered to be the "input" and "output" fields, respectively. Considering this, the integration of the coaxial subdomain equations yields

$$a_p(t,\omega_p) = e^{-i\omega_p(t-t_0)}a_p(t_0,\omega_p) - ig_p\int_{t_0}^{t} e^{-i\omega_p(t-t')}a_0(t')dt', \text{ for } t > t_0, \tag{27}$$

$$a_p(t,\omega_p) = e^{-i\omega_p(t-t_1)}a_p(t_1,\omega_p) + ig_p\int_{t}^{t_1} e^{-i\omega_p(t-t')}a_0(t')dt', \text{ for } t < t_1, \tag{28}$$

where t_0 is the initial condition time and t_1 is the final condition time.

Substituting each of the solutions for the coaxial subdomain of (27) and (28) into (25) results in

$$\frac{\partial a_0}{\partial t} = -i\omega_0 a_0 - i\sum_p g_p\int_{-\infty}^{\infty} e^{-i\omega_p(t-t_0)}a_p(t_0,\omega_p)d\omega_p - \sum_p\int_{-\infty}^{\infty} g_p^2\int_{t_0}^{t} e^{-i\omega_p(t-t')}a_0(t')dt'd\omega_p, \tag{29}$$

$$\frac{\partial a_0}{\partial t} = -i\omega_0 a_0 - i\sum_p g_p\int_{-\infty}^{\infty} e^{-i\omega_p(t-t_1)}a_p(t_1,\omega_p)d\omega_p + \sum_p\int_{-\infty}^{\infty} g_p^2\int_{t}^{t_1} e^{-i\omega_p(t-t')}a_0(t')dt'd\omega_p. \tag{30}$$

At this point, we can simplify the notation by defining $a_{\text{in},p}(t)$ and $a_{\text{out},p}(t)$ as

$$a_{\text{in},p}(t) = \frac{1}{\sqrt{2\pi}}\int_{-\infty}^{\infty} e^{-i\omega_p(t-t_0)}a_p(t_0,\omega_p)d\omega_p, \tag{31}$$

$$a_{\text{out},p}(t) = \frac{1}{\sqrt{2\pi}}\int_{-\infty}^{\infty} e^{-i\omega_p(t-t_1)}a_p(t_1,\omega_p)d\omega_p. \tag{32}$$

Further, we can make the Markov approximation to assume that g_p varies slowly enough over the frequency range of interest (nominally, the bandwidth of the cavity resonance) so that it can be factored out of the frequency integrals. Factoring g_p out at the center frequency of the cavity resonance and applying standard Fourier transform identities allows the final terms in (29) and (30) to simplify to be $\pi g_p^2 a_0(t)$ [11]. Combining these simplifications, we finally have that (29) and (30) become

$$\frac{\partial a_0}{\partial t} = -i\omega_0 a_0(t) - \sum_p (i\sqrt{2\pi}g_p a_{\text{in},p}(t) + \pi g_p^2 a_0(t)), \tag{33}$$

$$\frac{\partial a_0}{\partial t} = -i\omega_0 a_0(t) - \sum_p (i\sqrt{2\pi}g_p a_{\text{out},p}(t) - \pi g_p^2 a_0(t)). \tag{34}$$

At this point, it is convenient to exploit the linearity of the system to perform a time-harmonic analysis. Taking the Fourier transform of (33) and (34), we arrive at

$$-i\omega a_0(\omega) = -i\omega_0 a_0(\omega) - \sum_p (i\sqrt{2\pi}g_p a_{\text{in},p}(\omega) + \pi g_p^2 a_0(\omega)), \tag{35}$$

$$-i\omega a_0(\omega) = -i\omega_0 a_0(\omega) - \sum_p (i\sqrt{2\pi} g_p a_{\text{out},p}(\omega) - \pi g_p^2 a_0(\omega)). \tag{36}$$

Subtracting (36) from (35) results in what is typically referred to as a "boundary condition" in input-output theory at each coaxial subdomain, which in the frequency domain looks like

$$a_{\text{in},p}(\omega) - a_{\text{out},p}(\omega) = i\sqrt{2\pi} g_p a_0(\omega). \tag{37}$$

To find the scattering parameters within this formalism, we first eliminate the cavity mode in (35) by substituting into this equation using (37) evaluated for the second coaxial subdomain. Performing this, we arrive at

$$a_{\text{out},2}(\omega) = \frac{\big(\pi(g_1^2 - g_2^2) - i(\omega - \omega_0)\big) a_{\text{in},2}(\omega) - 2\pi g_1 g_2 a_{\text{in},1}(\omega)}{\sum_p \pi g_p^2 - i(\omega - \omega_0)}, \tag{38}$$

with a similar expression also able to be found in terms of the first coaxial subdomain. Since our analysis is classical, we can choose to turn one of the coaxial input fields "off" to compute the scattering parameters. Considering this, we can determine that the S_{22} and S_{21} are

$$S_{22} = \frac{a_{\text{out},2}(\omega)}{a_{\text{in},2}(\omega)} = \frac{\pi(g_1^2 - g_2^2) - i(\omega - \omega_0)}{\sum_p \pi g_p^2 - i(\omega - \omega_0)}, \text{ with } a_{\text{in},1}(\omega) = 0, \tag{39}$$

$$S_{21} = \frac{a_{\text{out},2}(\omega)}{a_{\text{in},1}(\omega)} = \frac{-2\pi g_1 g_2}{\sum_p \pi g_p^2 - i(\omega - \omega_0)}, \text{ with } a_{\text{in},2}(\omega) = 0, \tag{40}$$

which are characteristic of a Lorentzian intensity transfer function, as expected.

4. NUMERICAL RESULTS

The geometry considered for validating this formulation is shown in Fig. 1. The dimension of the cavity is $22.86 \times 10.16 \times 40\,\text{mm}^3$. The coaxial subdomains each have $a = 0.05\,\text{mm}$, $b = 1\,\text{mm}$, $\epsilon_r = 12.92$, and $\mu_r = 1$. Further, because of the symmetric positions of the coaxial probes and that the magnetic field for the dominant cavity mode is odd with respect to the center of the geometry we have that $g_1 = -g_2$. In our validation of the formalism, the length that the inner conductor protrudes into the cavity is varied from 0.05 mm to 1.5 mm. To account for the presence of this coaxial perturbation, spatial eigenmodes and eigenvalues are found for the cavity region using the finite element method (FEM). These numerical eigenmodes are then normalized and used to compute all relevant quantities involved in the input-output theory expressions. These results will be compared to standard driven FEM simulations for validation. All FEM analyses were performed with HFSS in this work.

To begin verifying the accuracy of the Hamiltonian, we first compute the full-width half-maximum (FWHM) of the intensity transmission function (i.e., $|S_{21}|^2$). From the input-output theory result, the g_p can be directly related to the decay rate of the cavity through a particular interface, with the overall result being that the FWHM in angular frequency units is

$$\text{FWHM} = \sum_p 2\pi g_p^2. \tag{41}$$

In Fig. 2(a), the computation of the FWHM via (41) is compared against that found by directly simulating the S_{21} of the geometry in HFSS, showing excellent agreement as a function of probe length. We also investigate the location of the center frequency of the cavity resonance as a function of probe length, shown in Fig. 2(b). We find more deviation here, but given the approximately constant offset over a wide range of probe lengths we attribute this error to numerical solution differences in HFSS rather than due to the projector-based formalism.

As a further check of the projector-based formalism, we compare the magnitude and phase of the S_{21} as a function of frequency directly between the input-output theory solution and the driven FEM results for a coaxial probe length of 0.75 mm in Fig. 3. To clearly show the similarity in the curves, we correct for the frequency offset shown in Fig. 2(b) first. After this, we see excellent

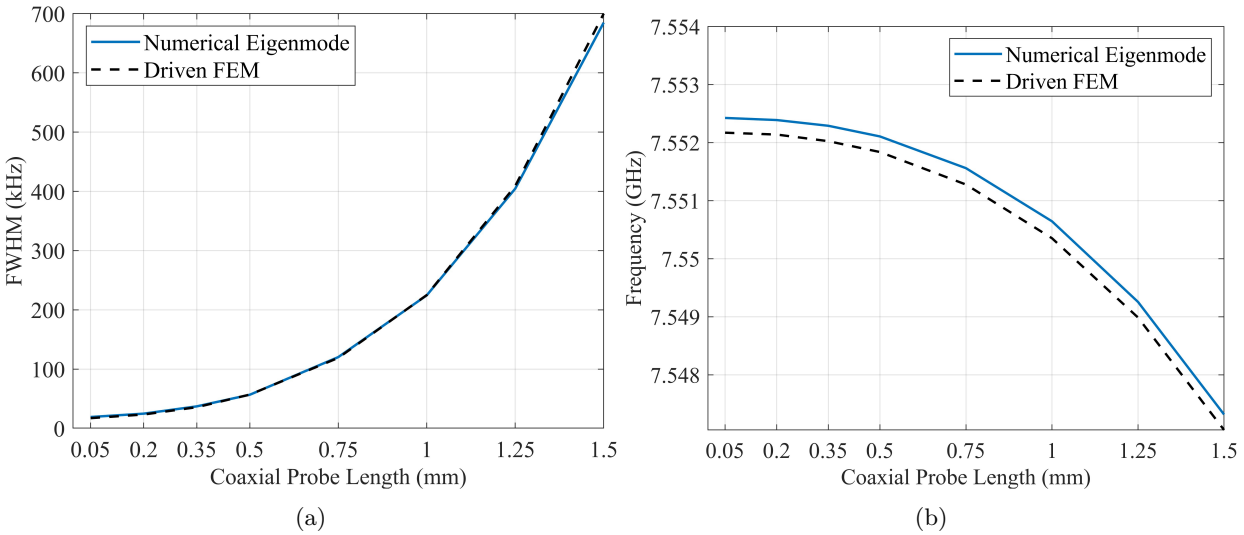

Figure 2: (a) Comparison of the transmission FWHM computed using numerical eigenmodes in the input-output theory formulation and directly computed from driven FEM. (b) Comparison of the resonant frequency from the numerical eigenmode and driven FEM simulations. Both (a) and (b) are plotted in linear frequency units.

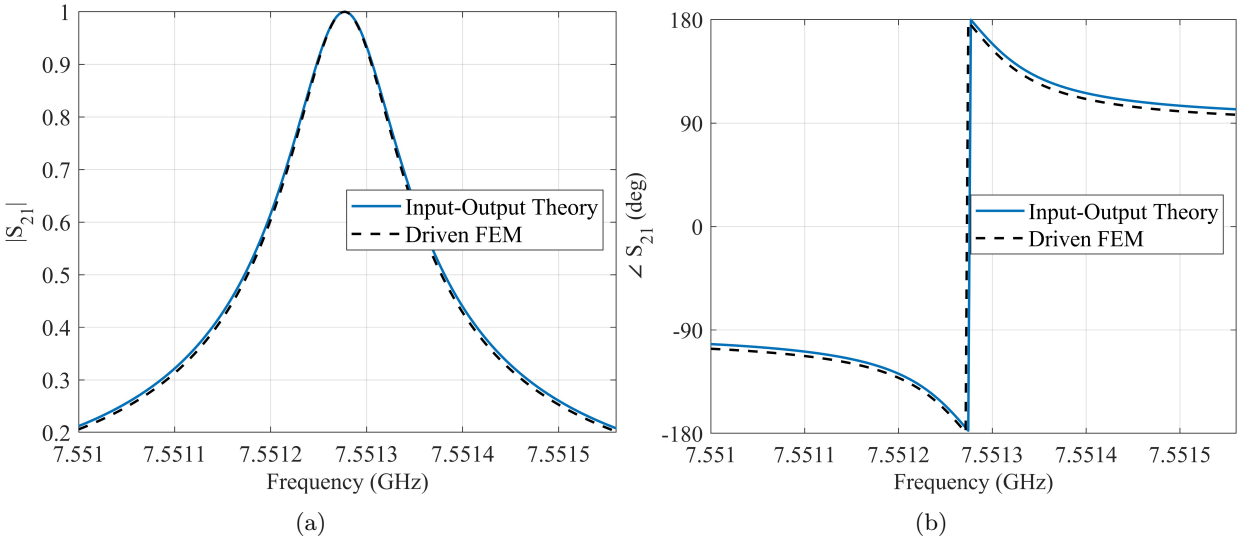

Figure 3: Comparison of the (a) magnitude and (b) phase of S_{21} for a coaxial probe length of 0.75 mm when using numerical eigenmodes in the input-output theory formulation and driven FEM simulations.

agreement between the two methods, with similar results found for all other coaxial probe lengths. It should also be noted that to achieve agreement in the phase plots in Fig. 3(b), we first must rederive our results using the same $e^{i\omega t}$ time convention used in HFSS and establish a single phase reference point at the starting frequency of the simulation. With these references set, we achieve very good agreement between methods, as shown in Fig. 3(b).

5. CONCLUSION

This work presented a full-wave Hamiltonian analysis method for a coaxial-fed rectangular waveguide cavity using a projector-based approach in the classical regime where its validity can be easily verified. Equations of motion were formulated for this system, and their analytical solution was shown using a classical version of input-output theory commonly used in quantum optics. This classical formulation was shown to be valid by comparing to standard FEM simulations, and due to its identical field-based characteristics to the quantum full-wave Hamiltonian proposed in [9] also validates relevant Hamiltonian terms in that formulation. Our future work will include incorporating a small dipole antenna into the cavity to validate the field-qubit coupling Hamiltonian given in

[9], as well as solving the full-wave quantum model in its entirety.

ACKNOWLEDGMENT

This material is based upon work supported by the National Science Foundation under Grant No. 2202389 and Purdue ECE Elmore Emerging Frontiers Center "The Crossroads of Quantum and AI."

APPENDIX

This section provides the details on the field mode profiles at different subdomains and corresponding normalization constants needed in field normalization. Here, we ignore the presence of the coaxial perturbations to illustrate the normalization process using the analytical cavity field expressions. However, to account for the coaxial perturbations inside the cavity we use numerical eigenmodes computed with FEM for the results presented in the main text. Due to the small nature of the perturbations, the analytical normalizations discussed in this appendix are still helpful for normalizing the numerical eigenmodes.

For cavity fields, it is common to separate the eigenmodes into TE and TM modes whose normalization needs to be considered separately. In each case, the normalized fields are expressed as

$$\mathbf{E}_k(\mathbf{r}) = \frac{1}{\sqrt{N_{u,k}}}\mathbf{u}_k(\mathbf{r}),\ \mathbf{H}_k(\mathbf{r}) = \frac{1}{\sqrt{N_{v,k}}}\mathbf{v}_k(\mathbf{r}), \tag{42}$$

where $\mathbf{u}_k$ and $\mathbf{v}_k$ are field modes before normalization and $N_{u,k}$ and $N_{v,k}$ are the normalization constants found via

$$N_{u,k} = \iiint \epsilon_r(\mathbf{r})\mathbf{u}_k^*(\mathbf{r})\cdot\mathbf{u}_k(\mathbf{r})dV,\ N_{v,k} = \iiint \mathbf{v}_k^*(\mathbf{r})\cdot\mathbf{v}_k(\mathbf{r})dV. \tag{43}$$

Now, for TE modes, the unnormalized z-component that all other field components may be computed from would be

$$v_z = H_{mnp}\cos\frac{m\pi x}{a}\cos\frac{n\pi y}{b}\sin\frac{p\pi z}{d}, \tag{44}$$

where the m, n, and p are integers in the classical electromagnetics conventions, H_{mnp} is a constant, and $k_{t,mn} = \sqrt{(\frac{m\pi}{a})^2 + (\frac{n\pi}{b})^2}$. The unique combinations of m, n, and p corresponds to the single mode index k used in the cavity subdomain in the main paper. Then, the normalization constants for electric and magnetic fields can be found to be

$$N_{u,k} = -\epsilon_r\frac{(H_{mnp}\,\omega\mu)^2}{k_{t,mn}^2}\frac{abd}{C_n}, \tag{45}$$

$$N_{v,k} = \Big(\frac{H_{mnp}}{k_{t,mn}^2}\Big)^2\Big\{\Big(\frac{m\pi}{a}\frac{p\pi}{d}\Big)^2 + \Big(\frac{n\pi}{b}\frac{p\pi}{d}\Big)^2 + \Big(\frac{m\pi}{a}\Big)^4 + 2\Big(\frac{m\pi}{a}\frac{n\pi}{b}\Big)^2 + \Big(\frac{n\pi}{b}\Big)^4\Big\}\frac{abd}{C_n}, \tag{46}$$

where the factor C_n reduces down to a smaller number if any one of m, n, or p is 0 as in

$$C_n = \begin{cases} 8, & \text{if } m\neq 0,\ n\neq 0, \text{ and } p\neq 0, \\ 4, & \text{if } m=0,\ n\neq 0, \text{ and } p\neq 0; \text{ or } m\neq 0,\ n=0, \text{ and } p\neq 0; \text{ etc.} \end{cases} \tag{47}$$

For TM modes, the unnormalized z-component that all other field components may be computed from would be

$$u_z = E_{mnp}\sin\frac{m\pi x}{a}\sin\frac{n\pi y}{b}\cos\frac{p\pi z}{d}, \tag{48}$$

where E_{mnp} is a constant. Then, the normalization constants for electric and magnetic fields are

$$N_{u,k} = \epsilon_r\Big(\frac{E_{mnp}}{k_{t,mn}^2}\Big)^2\Big\{\Big(\frac{m\pi}{a}\frac{p\pi}{d}\Big)^2 + \Big(\frac{n\pi}{b}\frac{p\pi}{d}\Big)^2 + \Big(\frac{m\pi}{a}\Big)^4 + 2\Big(\frac{m\pi}{a}\frac{n\pi}{b}\Big)^2 + \Big(\frac{n\pi}{b}\Big)^4\Big\}\frac{abd}{C_n}, \tag{49}$$

$$N_{v,k} = -\frac{(E_{mnp}\,\omega\epsilon)^2}{k_{t,mn}^2}\frac{abd}{C_n}, \tag{50}$$

and C_n is defined as in (47).

For the coaxial subdomain, the TEM, TE, and TM modes all can exist. Here, we only consider the TEM mode explicitly since for our geometry all the higher order modes are significantly in the cutoff region (i.e., there is only one fixed λ index considered). Then, the unnormalized field expressions for the TEM mode expressed in a local cylindrical coordinate system are

$$\mathbf{u}_{\lambda p} = \frac{V_0}{\rho\ln(b/a)}\cos\Big(\frac{\omega_{\lambda p}}{c}z\Big)\hat{\rho}, \tag{51}$$

$$\mathbf{v}_{\lambda p} = -\frac{I_0}{\rho}\sin\Big(\frac{\omega_{\lambda p}}{c}z\Big)\hat{\phi}, \tag{52}$$

where c is the speed of light in the coaxial subdomain, b is the length of the outer radius, and a is the length of the inner radius of the coaxial line. The V_0 and I_0 are constant amplitudes. Note that the z-dependence of the modes is fixed by the PMC boundary condition located at $z = 0$ in the local corrdinate system (see Fig. 1). The normalized fields are explicitly defined similar to (42), and the normalization constants become

$$N_{u,\lambda p} = \epsilon_r\frac{|V_0|^2}{\ln(b/a)}\pi^2 c, \tag{53}$$

$$N_{v,\lambda p} = \mu_r|I_0|^2\ln(b/a)\pi^2 c. \tag{54}$$

REFERENCES

1. F. Arute, K. Arya, R. Babbush, D. Bacon, J. C. Bardin, R. Barends, R. Biswas, S. Boixo, F. G. Brandao, D. A. Buell *et al.*, "Quantum supremacy using a programmable superconducting processor," *Nature*, vol. 574, no. 7779, pp. 505–510, 2019.
2. Y. Wu, W.-S. Bao, S. Cao, F. Chen, M.-C. Chen, X. Chen, T.-H. Chung, H. Deng, Y. Du, D. Fan *et al.*, "Strong quantum computational advantage using a superconducting quantum processor," *Physical Review Letters*, vol. 127, no. 18, p. 180501, 2021.
3. P. Jurcevic, A. Javadi-Abhari, L. S. Bishop, I. Lauer, D. F. Bogorin, M. Brink, L. Capelluto, O. Günlük, T. Itoko, N. Kanazawa *et al.*, "Demonstration of quantum volume 64 on a superconducting quantum computing system," *Quantum Science and Technology*, vol. 6, no. 2, p. 025020, 2021.
4. R. Acharya, I. Aleiner, R. Allen, T. I. Andersen, M. Ansmann, F. Arute, K. Arya, A. Asfaw, J. Atalaya, R. Babbush *et al.*, "Suppressing quantum errors by scaling a surface code logical qubit," *Nature*, vol. 614, no. 7949, pp. 676–681, Feb 2023.
5. P. Krantz, M. Kjaergaard, F. Yan, T. P. Orlando, S. Gustavsson, and W. D. Oliver, "A quantum engineer's guide to superconducting qubits," *Applied Physics Reviews*, vol. 6, no. 2, p. 021318, 2019.
6. A. A. Houck, J. A. Schreier, B. R. Johnson, J. M. Chow, J. Koch, J. M. Gambetta, D. I. Schuster, L. Frunzio, M. H. Devoret, S. M. Girvin *et al.*, "Controlling the spontaneous emission of a superconducting transmon qubit," *Physical Review Letters*, vol. 101, no. 8, p. 080502, 2008.
7. S. E. Nigg, H. Paik, B. Vlastakis, G. Kirchmair, S. Shankar, L. Frunzio, M. Devoret, R. Schoelkopf, and S. Girvin, "Black-box superconducting circuit quantization," *Physical Review Letters*, vol. 108, no. 24, p. 240502, 2012.
8. Z. K. Minev, Z. Leghtas, S. O. Mundhada, L. Christakis, I. M. Pop, and M. H. Devoret, "Energy-participation quantization of Josephson circuits," *npj Quantum Information*, vol. 7, no. 1, pp. 1–11, 2021.
9. T. E. Roth and W. C. Chew, "Macroscopic circuit quantum electrodynamics: A new look toward developing full-wave numerical models," *IEEE Journal on Multiscale and Multiphysics Computational Techniques*, vol. 6, pp. 109–124, 2021.
10. C. Viviescas and G. Hackenbroich, "Field quantization for open optical cavities," *Physical Review A*, vol. 67, no. 1, p. 013805, 2003.
11. D. F. Walls and G. J. Milburn, *Quantum Optics*. Springer Science & Business Media, 2007.